Materials Research Bulletin 191 (2025) 113546

Contents lists available at ScienceDirect

Materials Research Bulletin

journal homepage: www.elsevier.com/locate/matresbu

Research Papers

Chemical approach to achieve sodiated alloying anode for direct application in Na-ion battery

Luca Minnetti [a,b,1], Edoardo Barcaro [c,1], Leonardo Sbrascini [a], Francesco Nobili [a,b,*], Jusef Hassoun [c,d,*]

[a] School of Sciences and Technologies – Chemistry Division, University of Camerino, Via Madonna delle Carceri ChIP, Camerino 62032, Italy
[b] GISEL – Centro di Riferimento Nazionale per i Sistemi di Accumulo Elettrochimico di Energia, INSTM, Firenze 50121, Italy
[c] Department of Chemical, Pharmaceutical and Agricultural Sciences, University of Ferrara, Via Fossato di Mortara 17, Ferrara 44121, Italy
[d] Graphene Labs, Istituto Italiano di Tecnologia, via Morego 30, Genoa 16163, Italy

ARTICLE INFO

Keywords:
Sodium layered oxide
NCAM
Sodium alloy
Na-SnC
Chemical sodiation
Na-ion battery

ABSTRACT

Metal-free Na-ion battery with sodium-deficient cathodes such as layered oxides foresees a careful tuning of the sodium content at the negative side. We exploit a versatile chemical strategy to get sodiated versions of a tin-carbon (Sn-C) alloying electrode for application in full-cell. The process is performed by capillary contacting Sn-C and sodium metal to trigger the chemical alloying, which leads to the Na_xSn-C electrode. The success of the reaction is monitored by X-ray diffraction (XRD) and Raman spectroscopy, while the morphological changes are exploited by scanning electron microscopy (SEM). The achieved Na_xSn-C electrode is advantageously used as anode in combination with Al-doped, Na-defective layered oxide in a full-cell. The battery is cycled galvanostatically and fully investigated by electrochemical impedance spectroscopy (EIS). The optimized Sn-C|NCAM cell reveals maximum capacity of 120 mAh g_{cat}^{-1}, energy and power density respectively of 300 Wh kg_{cat}^{-1} and 650 W kg_{cat}^{-1}, and lifespan extended over 250 cycles.

1. Introduction

Na-ion battery so far appeared as the less expensive and more accessible analogue of the most widely diffused Li-ion one, based on the ions exchange by a *rocking-chair* mechanism [1,2]. However, the exploitation of such an intriguing reaction, which can efficiently move the lithium ions from cathode to anode for storing energy and back to get power, appeared relevantly more complex in the sodium environment than lithium [3,4]. Indeed, one of the most diffused and efficient cathodes for Na-cell is represented by the transition-metal layered oxide that can be sodium deficient or sodium rich, with O_2, P_2, P_3 or P_3' structures [5–10]. This variety of configurations typically requires a sodium metal anode to compensate the alkali metal content into the cathode structure [11]. On the other side, olivine-type electrodes have represented so far the cheapest, still well-performing, cathode for actual application in Li-ion batteries due to the modest economic and environmental impact [12,13]. However, the synthetic pathways for achieving the sodium analogue of these electrodes typically lead to the predominant formation of the electrochemically inactive maricite structure instead of the olivine triphylite one [14–16]. Hence, electrochemical de-lithiation from Li-based olivines can be used for removing the alkali metal from the polyanionic framework, to finally get a version of the cathode host framework, which can operate reversibly when coupled in sodium metal battery [17]. Therefore, a balanced Na-ion battery using at the cathode side either layered oxides or electrochemically converted olivines mandatory foresees the adequate pre-storing of Na reservoir in anodes, in analogy to what already adopted for Li-ion cells, in particular using the Li-alloying electrodes [18–21]. Among the alloying materials suitable for this activation process, Si, Sn and Sb revealed the most promising features both in lithium [22–28] and in sodium batteries [29–35]. Moreover, the study of pre-sodiation of both cathode and anode acquired relevant importance for Na-ion batteries, due to the above mentioned sodium deficiency at the cathode side and initial irreversibility due to solid electrolyte interphase (SEI) formation at the anode side [36]. In these regards, different strategies have been adopted for the pre-sodiation of electrodes, including electrochemical activation of anode and cathode [16,36,37], chemical or mechanochemical treatments [38–40], as well as the use of sacrificial Na salts as the additives

* Corresponding authors.
E-mail addresses: francesco.nobili@unicam.it (F. Nobili), jusef.hassoun@unife.it (J. Hassoun).
[1] These authors contributed equally to this work.

https://doi.org/10.1016/j.materresbull.2025.113546
Received 14 April 2025; Accepted 9 May 2025
Available online 9 May 2025

[41–43]. Relevantly, the high conductivity of metallic Sn and Sb can allow either the typical electrochemical sodiation by charging/discharging in half cell to retrieve the electrode for full-cell application [27], or a more scalable and appealing pathway in which the Na-metal alloy is directly achieved by mechanochemical treatments [44]. Herein we exploit a direct mechanical treatment of a previously prepared Sn-C anode [45] for application in a full Na-ion cell using the $Na_{0.48}Al_{0.03}Co_{0.18}Ni_{0.18}Mn_{0.47}O_2$ (NCAM) layered cathode described elsewhere [11,46]. The anode can operate in Na-cell according to the alloying mechanism with a capacity over 100 mAh g^{-1}, however with an initial irreversibility exceeding 50 % of the steady state value, which is typical of this class of materials [17,23]. Instead, the cathode can deliver in half-cell about 180 mAh g^{-1}, however with an initial charge limited to only 60 % of the maximum value [10,11]. The compensation of the initial sodium deficiency at the cathode side and of the initial irreversibility of the anode is originally exploited by a pre-treatment process of the Sn-C anode consisting of mechanical capillary contact with sodium metal. Tuning the contact time and pressure allowed the achievement of various degrees of anode sodiation, as monitored by XRD, Raman spectroscopy and confirmed electrochemically. The most suitable condition is then adopted to get adequate Na_xSn-C anode for the application in the full-cell with the selected NCAM cathode, which is subsequently cycled by concomitantly monitoring the single electrodes as well as the full-cell voltage, and characterized by EIS and *ex-situ* SEM. Subsequently, an optimization of the Sn-C|NCAM full-cell setup has been carried out to improve the performances and avoid side reactions or inefficiency, thus leading to an enhanced battery. This full-cell has been characterized in terms of rate capability, interfacial features, and long term cycling ability. The outcomes of this work suggested the mechanical pre-sodiation a well-suitable approach to scale up the Na-ion battery and achieve a sustainable energy storage.

2. Materials and methods

Sn-C was synthetized as reported in previous paper [45]. In brief, resorcinol was mixed with formaldehyde and sodium carbonate as catalyst to obtain a dark orange hydrogel, which was aged, ground, washed with water and then immersed in tert-butyl alcohol and filtered. Afterwards, the particles were mixed overnight with the organometallic tin source tributylphenyltin (TBPT), recovered, placed in an oven under Ar-H_2 flux, and heated at 700 °C for 2 h. NCAM was synthetized through a co-precipitation method, according to previous works [10,46], by dissolving nitrate precursors of Al, Co, Ni, and Mn in deionized water to obtain a solution with a Al/Co/Ni/Mn molar ratio of 1:2:2:4.5. The corresponding hydroxide was precipitated from the solution using NaOH, filtered, washed with deionized water, and dried. This precursor was mixed with NaOH in 1:1 molar ratio, calcinated at 500 °C, grinded, pelletized, calcinated again at 1000 °C in a dry air flow, rinsed with deionized water, and dried under vacuum at 100 °C overnight.

The electrode slurries were prepared by dispersing the active material (either NCAM or Sn-C), polyviniylidene fluoride (PVDF 6020 Solef®) binder, and carbon black (Super P carbon, Timcal), mixed by the 8:1:1 wt ratio in N-methyl-2-pyrrolidone (NMP, Sigma-Aldrich), and then stirred at room temperature until homogenization (about 2 h). The obtained slurries were cast by a doctor blade tool on either aluminum (thickness of 20 μm, MTI Corporation) for NCAM or scratched copper foils (thickness of 30 μm, MTI Corporation) for Sn-C and subsequently dried for 3 h on a hot plate at 70 °C, cut into disks of 10 mm-diameter, and dried again for 3 h at 110 °C under vacuum to remove possible traces of water and NMP solvent. Prior to vacuum drying, NCAM electrodes were pressed with a hydraulic press (Silfradent) for 30 s at 110 bar, while the SnC tape was calendared by using an MSK-2150 Rolling Machine (MTI Corp.) to achieve a thickness within the range of 100 – 110 μm. Carbon/PVDF electrodes coated on scratched Cu foil, labelled SPC-Cu, were prepared to determine the electrolyte cathodic stability. These —SPC-Cu electrodes were achieved by doctor blade casting procedure described above, using carbon black (Super P carbon, Timecal) and PVDF binder in the 80:20 wt. % ratio, cut into 10 mm disks, and dried at 110 °C for 3 h under vacuum. Sn-C electrodes were sodiated via capillary contact between the material and sodium metal inside an Ar-filled glove box: the Sn-C electrode was placed in contact with a sodium metal disk wetted with a 1 M solution of sodium perchlorate ($NaClO_4$) dissolved in propylene carbonate (PC, battery grade, Sigma-Aldrich) with 3 % in weight of fluoroethylene carbonate (FEC, battery grade, Solvionic) and placed in between two Petri dishes. Subsequently, a 1 kg weight was stacked on the electrode and the system was allowed to chemically react until the target time was reached (1 h, 2 h, 6 h, 10 h, and14 h). The final active material loading of Sn-C electrodes employed in the capillary sodiation studies was about 2.0 mg cm^{-2}, as normalized to the electrode geometric area (0.785 cm^2). It is worth mentioning that the activation time of the Sn-C electrodes in this work may be subjected to *ad hoc* modulation according to the active material loading, pressure, electrode, and electrolyte composition adopted during the process. Two-electrode Swagelok T-type sodium half-cells were assembled by stacking a 10mm-diameter working electrode (either pristine or sodiated Sn-C anode, or NCAM cathode), a 10mm-diameter sodium metal disk (Sigma Aldrich, 99 %) as counter electrode, and a 10 mm-diameter glass fiber (Whatman® GF/B) disk as separator. A three-electrode Swagelok T-type sodium cell was prepared using a 10 mm-diameter SP-Cu working electrode, a 10 mm-diameter sodium metal counter electrode, a 10 mm-diameter glass fiber (Whatman® GF/B) disk as the separator, and an additional 10 mm sodium metal disk as reference electrode. Three-electrode Swagelok T-type full-cells were assembled by stacking a NCAM cathode, a 2 h sodiated Sn-C anode, one glass fiber (Whatman® GF/B) disk as the separator, and an additional sodium metal disk as the reference electrode placed at the top side of the T-cell. Optimized setup CR2032 coin-type full-cells (MTI Corporation) were assembled by using a 10 mm-diameter NCAM cathode, a 10 mm-diameter Sn-C anode activated for 30 min, and a 16 mm-diameter glass fiber (Whatman® GF/B) disk as the separator (the active material loading of the electrodes is reported in the respective figure caption whenever a full-cell is reported). All the full-cells were prepared by using negative to positive (N/P) capacity ratios of 1.1, as determined by considering mass loadings and specific capacities of the two electrodes. In every cell configuration, 1 M solution of $NaClO_4$ in PC + 3 % wt FEC was used as electrolyte. The sodiated Sn-C electrodes were used without any other treatment before assembling the cells. All cells were assembled and sealed inside an Ar-filled glovebox (MBraun, O_2 and H_2O content lower than 1 ppm).

XRD patterns of the pristine and activated Sn-C electrodes, leaned on a glass sample holder and sealed with Kapton tape, were collected through a Bruker D8 Advance instrument using a Cu K_α source and a graphite monochromator of the diffracted beam by performing scans in the 2θ range from 27° to 47° at a rate of 4 s $step^{-1}$ with a step size of 0.02°. SEM images of the pristine and sodiated (14 h) Sn-C electrodes and EDS spectra were collected through a Zeiss Sigma 300 FE-SEM (5 keV beam) equipped with Bruker QUANTAX EDX detector. Raman spectroscopy was performed on micrometric Sn powder (< 45 μm particle size, 99.8 % trace metal basis, Sigma-Aldrich), pristine, and sodiated Sn-C electrodes, by using a Czerny-Turner spectrometer (iHR320 Horiba Scientific) equipped with a diffraction grating of 1800 grooves mm^{-1} and a laser source with $\lambda = 532$ mm. Before the analysis, all the electrodes, recovered after chemical process, were washed with dimethyl carbonate (DMC) solvent and dried under vacuum for 30 min. For Raman analysis all the samples were placed into a sealed sample holder in Ar atmosphere.

The activated Sn-C electrodes were cycled in two-electrode Na|Sn-C half-cells at the constant current of 15 mA g^{-1} in the voltage range of 0.01 – 2.0 V for the capillary sodiation process study. Additional galvanostatic cycling tests were performed in two-electrode Na|NCAM and Na|Sn-C half-cells in the 1.4 – 4.6 V and 0.01 – 1.5 V voltage ranges, respectively, at the constant current rate of 50 mA g^{-1} for NCAM and 100 mA g^{-1} for the Sn-C electrode sodiated for 2 h. Full Sn-C|NCAM 3-

electrodes T-type cells were galvanostatically cycled at the constant current of 15 mA g_{cat}^{-1} in the 1.0 – 4.5 V voltage range by adopting the constant current-constant voltage (CCCV) mode with constant voltage step during charge at 4.5 V until a residual current value of 3.75 mA g_{cat}^{-1} was reached. Full Sn-C|NCAM coin-type cells were cycled at the constant current rate of 120 mA g_{cat}^{-1} in the following voltage ranges: 1.0 – 4.1 V, 1.0 – 4.0 V, 1.5 – 4.5 V by adopting the CCCV mode at 4.5 V until a residual current value of 12 mA g_{cat}^{-1} was reached. A rate capability test was conducted on an additional Sn-C|NCAM coin-type full-cell by increasing the current from 1 C (considered in this work as 50 mA g_{cat}^{-1} for convenience) to 2 C, 3 C, 4 C, and 5 C every 5 cycles and lowering back to 1 C after 25 cycles in the 1.0 – 4.0 V voltage range. Long-term galvanostatic cycling was conducted on the same cell at the constant current of 200 mA g_{cat}^{-1} in the 1.0 – 4.0 V voltage range, by adopting the CCCV mode at 4.0 V until a residual current value of 50 mA g_{cat}^{-1} was reached. EIS measurements were carried out on the three-electrode Sn-C|NCAM T-type cell at the OCV condition and after 1, 8, and 10 galvanostatic cycles by superimposing an alternate voltage signal of 30 mV in the 500 kHz – 100 mHz frequency range (1 V bias voltage). Additional EIS measurements were performed on the Sn-C|NCAM coin-type cell at the OCV condition, and after the rate capability test. All the Nyquist plots recorded by EIS were analyzed through non-linear least squares (NLLS) fitting method by using the RelaxIS3 software (rhd instruments), and only fits with χ^2 value of the order of 10^{-4} or lower were accepted [47,48]. The distribution of relaxation times (DRT) functions were calculated after subtracting the low-frequency diffusion region, by using the software RelaxIS3. The λ-factor for the DRT analysis was optimized according to Tikhonov regularization, by calculating the sum of squared residuals (SSR) vs. λ, and assuming a Gaussian distribution [49,50]. The charge/discharge cycling tests were performed by a MACCOR series 4000 battery test system, while the EIS measurements were carried out by using a VersaSTAT MC Princeton Applied Research (PAR, AMETEK) instrument. All the data were recorded at room temperature (25 °C). All potentials are given vs. Na^+/Na redox couple (E = –2.71 vs. SHE). Ex-situ SEM images of pristine and cycled Sn-C and NCAM electrodes were collected as above described.

3. Results and discussion

In order to minimize the relevant irreversible capacity of Na-alloying electrodes, such as in Sn-C during the first cycle, that limits their direct use in full Na-ion cell without the proper treatment [17], we originally exploit here a strategy consisting of capillary contact between the electrode and sodium metal wet by the electrolyte, in order to obtain a chemical partial pre-sodiation. The cycling response and the structural features are reported in Fig. 1. The related galvanostatic tests are

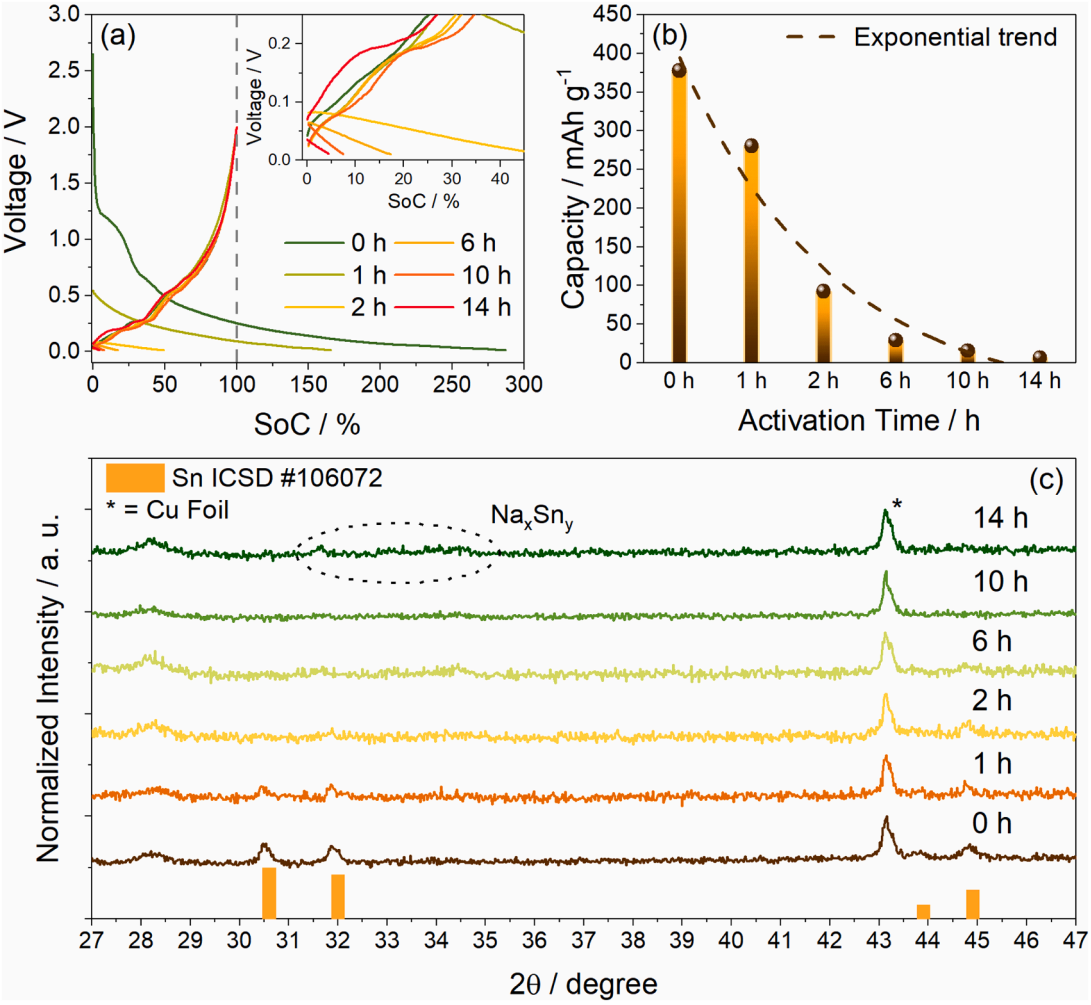

Fig. 1. Electrochemical and structural characterization of Sn-C samples with different sodiation times. (a) Voltage profiles as a function of SoC%, corresponding to the degree of sodiation (see Fig. S1 in Supporting Information for related galvanostatic profiles), with magnification of the low SoC% region in the inset. Tests performed by using a constant current of 15 mA g^{-1} in the 0.01 – 2.0 V voltage range. (b) First discharge (Na-alloying) capacity values at corresponding sodiation time with related exponential trend (dashed line). (c) XRD patterns of sodiated Sn-C samples compared to corresponding reference diffractogram of Sn (ICSD #106072). Room temperature (25 °C). See Materials and methods section for acronyms.

performed at a current of 15 mA g^{-1} between 0.01 and 2.0 V on electrodes contacted with Na for various times to assess the actual chemical sodiation degree vs. contact time. Fig. 1a shows the obtained voltage profiles as a function of the percent state of charge (SoC%). The SoC% values are calculated for each cell as the percent ratio of the first discharge (Na-alloying) capacity to the first charge (Na-dealloying) reversible capacity. Magnification of the low SoC% region is reported in the inset, while **Fig. S1** in Supporting Information shows the corresponding galvanostatic voltage profiles as a function of the actual specific capacity (i.e., E /V vs. capacity /mAh g^{-1}). The discharge capacity of the cell using the pristine Sn-C (0 h of sodiation) shows an irreversibility exceeding by 250 % the reversible value (~150 mAh g^{-1} in **Fig. S1**), thus indicating SoC% of 250 %. This relevant side capacity is mainly due to the concomitant electrolyte decomposition and electrode structural re-organization during first discharge, which is a characteristic of this type of electrodes [17,51]. As the time of contact between Na metal and Sn-C increases, the SoC% shrinks to reach 170 % for 1 h of sodiation, and less than 5 % for 14 h of sodiation, thus suggesting the

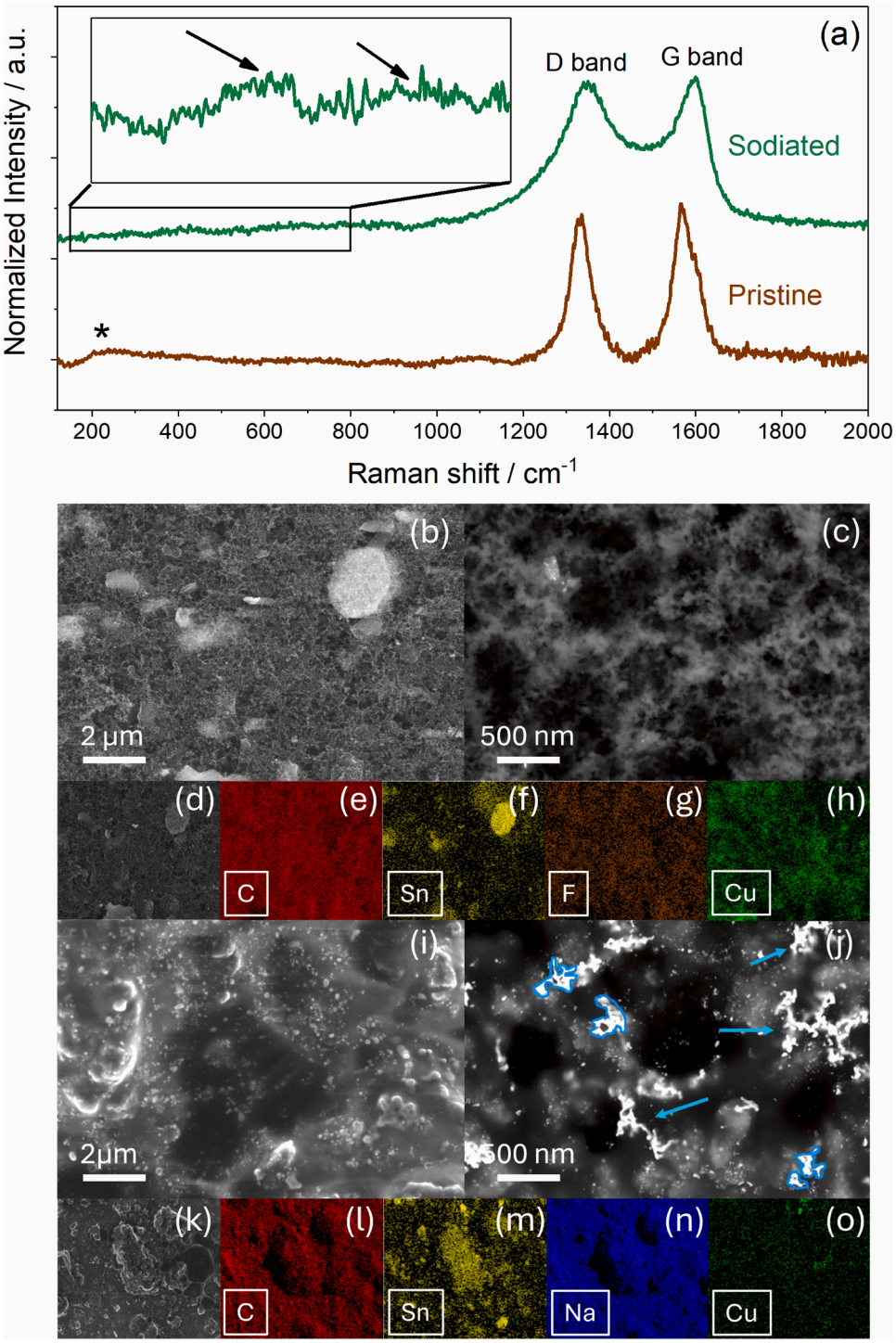

Fig. 2. Characterization of the pristine and sodiated (14 h) Sn-C electrodes. (a) Raman spectra recorded in the 150 – 2000 cm^{-1} range. Indexed peaks identify specific transitions identifications. SEM images at different magnifications of (b-d) pristine and (i-k) sodiated electrodes. In details: (c, j) backscattered electrons images. SEM-EDS elemental maps of (e, l) C, (f, m) Sn, (h, o) Cu, (g) F, and (n) Na for (e-h) pristine and (l-o) sodiated electrodes. See Materials and methods section for acronyms.

gradual suppression of the irreversible capacity, and the concomitant increase of reversible Na storage into the Sn-C structure by progressive chemical alloying. This behavior is also evidenced in Fig. 1b, which shows that the values of the first discharge capacity decrease upon chemical activation time by approximately following an exponential function (dashed line). On the other hand, the effectiveness of Na-Sn alloying is demonstrated by the XRD patterns of the sodiated Sn-C samples reported in Fig. 1c, that reveal the gradual disappearance of the metallic Sn reflections at 2θ of 30.5°, 31.9°,43.8°, and 44.8° (reference ICSD #106072), and the concomitant formation of weak signals attributed to a Na_xSn_y alloy at 2θ between 31.5° and 35° [17]. This response well suggests the tunability of the chemical sodiation process adopted in this work for possible application of the alloying electrode in combination with a vast array of cathodes, that may require different sodiation degree, such as layered oxides [10], olivines [16], and Na-conversion materials [52].

Fig. 2 depicts the structural and morphological changes of the Sn-C electrodes upon 14 h of sodiation described above, exploited by Raman spectroscopy and SEM/EDS. Prior to the analysis on electrodes, a Raman spectrum of micrometric Sn powder is collected (see **Fig. S2** in Supporting Information) in order to achieve a reference for metallic tin signals, which are centered at about 143 and 211 cm^{-1} [53]. The Raman spectra recorded for pristine, and sodiated Sn-C (Fig. 2a) indicate the presence of two strong bands at 1350 and 1600 cm^{-1}, due to D and G vibrations of the carbon matrix. Nevertheless, the pristine electrode (brown line) shows a weak peak around 200 cm^{-1} (indexed with asterisk) ascribed to the vibrational transition of Sn, while in the sodiated sample (green line) this peak almost vanishes. Furthermore, the magnified region between 150 and 800 cm^{-1}reveals for the sodiated sample two additional indexed peaks, possibly ascribed to residual $NaClO_4$ salt and product of the SEI formed at the Sn-C surface after the direct reaction with Na metal [53,54]. On the other hand, the SEM images at different magnifications of the pristine Sn-C (Fig. 2b–d) and of the sodiated one (Fig. 2i–k) depict changes of the typical submicrometric agglomerated morphology principally occurring at the material surface. These changes are in part evidenced by the rise of bright spots, highlighted by blue circles and arrows in Fig. 2j, likely accounting for the presence of sodium at the activated Sn-C surface. The EDS elemental maps collected on the SEM of the bare Sn-C in Fig. 2d show the expected presence of C (Fig. 2e) and Sn (Fig. 2f) components of the active material, Cu (Fig. 2h) of the support, and F (Fig. 2 g) of the polymeric binder used to form the electrode tape. Instead, F is missing in the maps collected on the SEM of the sodiated electrode of Fig. 2k while Cu is weakened (Fig. 2o), likely due to the surface covering by SEI. Furthermore, Na is detected (Fig. 2n) alongside with C (Fig. 2l) and Sn (Fig. 2m), thus accounting for the Sn-C sodiation.

The Na deficiency in the NCAM cathode studied in a preliminary work [10] would not allow the use of a typical anode without any Na-reservoir in its structure, necessary for allowing the complete discharge of the latter during the subsequent cycles in a possible full-cell combining the two materials. Therefore, among the pre-sodiation conditions of the Sn-C shown in Fig. 1b, a treatment time of 2 h has been initially selected as the most suitable for achieving a sufficient Na^+-reservoir to allow the proper operation of a full-cell combining this anode with the NCAM cathode as reported in Fig. 3. The time evolution of the full-cell voltage during galvanostatic cycling at a current of 15 mA g_{cat}^{-1} in the 1.0 – 4.5 V range is reported in Fig. 3a (black line), in addition to the voltage signatures of Sn-C (red line) and the NCAM (blue line), collected separately using a Na reference electrode to help a better understanding of the concomitant contributions of anode and cathode. Remarkably, the first charge profile of the full-cell depicts the combination of the partial de-sodiation of Na-deficient NCAM and of the

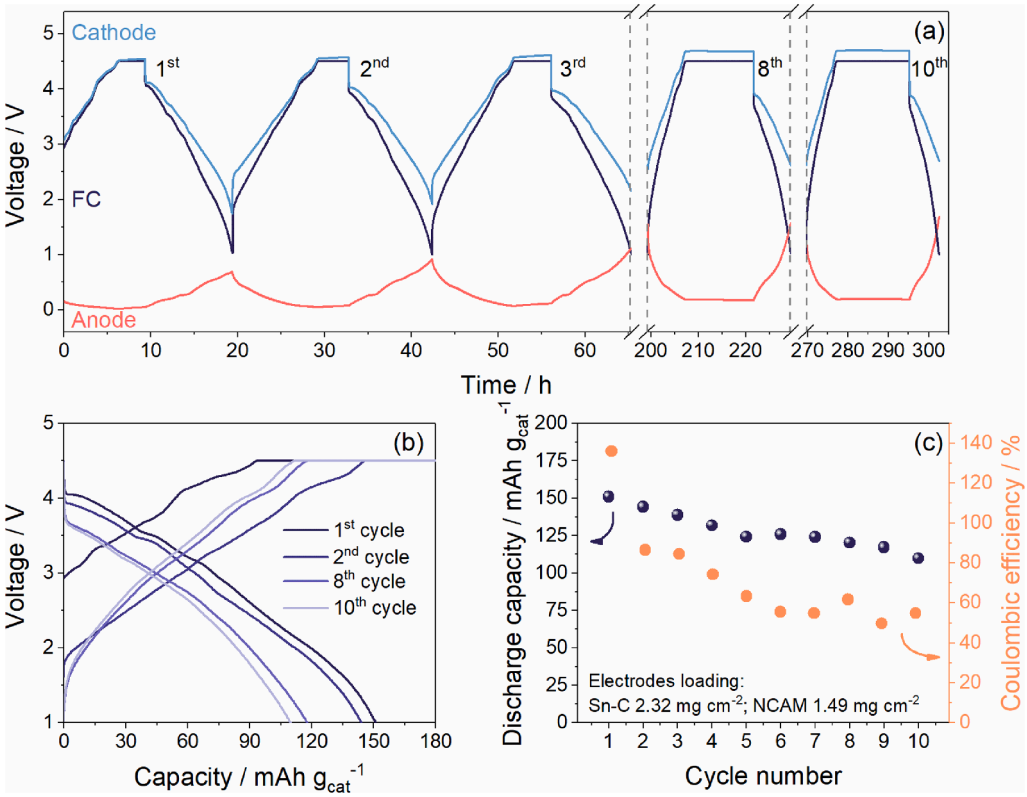

Fig. 3. (a) Time evolution of the Sn-C anode and the NCAM cathode voltage concomitantly collected by using an additional Na reference electrode, and of the corresponding Sn-C|NCAM full-cell. (b) Voltage profiles and (c) capacity trend (right y-axes shows coulombic efficiency) of the Sn-C|NCAM full-cell cycled at the constant current rate of 15 mA g_{cat}^{-1} in the 1.0 – 4.5 V voltage range. Measurement performed with an additional current voltage step at 4.5 V held until a current value of 3.75 mA g_{cat}^{-1} was reached (CCCV mode). Room temperature (25 °C). See Materials and methods section for acronyms.

corresponding sodiation of Sn-C. Subsequently, the cell reversibly operates with a voltage showing sloping signature combining the charge/discharge curves of anode and cathode for over 10 cycles, with initial capacity as high as 150 mAh g_{cat}^{-1} and a final value of about 110 mAh g^{-1}, as evidenced either by the corresponding voltage profile in Fig. 3b and the cycling trend in Fig 3c. However, the full-cell reveals a low coulombic efficiency (Fig 3c), fluctuating from 51 to 85 %, likely due to the reactivity of the electrodes, particularly the anode where the presence of Na metal clusters could induce a larger irreversibility with the electrolyte due to parasitic reactions. It is worth noting that the shape of the voltage profiles changes from the initial cycles to the 10th cycle as a consequence of the above mentioned low efficiency of the full-cell, thus leading to the instability of the battery and to the consequent fast capacity fade, which is partially mitigated by the CCCV mode [46,55]. On the other hand, the low efficiency of the full-cell progressively triggers metallic sodium deposition below 0 V on the anode surface (see red line in Fig. 3a at the 8th and 10th cycles). This undesired process, which is actually promoted by the relatively high charge cut-off, suggests the need for optimization of the galvanostatic cycling protocol. Overall, the results of Fig. 3 indicate the feasible cathode/anode setup in terms of the N/P ratio (i.e., 1.1), and the suitability of the chemical sodiation of the Sn-C electrode for achieving reversible operation of the full-cell. The data also suggest the need for a better tuning of the electrolyte as well as of the cycling condition, to get a higher efficiency and increase the full-cell stability and cycle life [56,57].

To shed light on the modification upon cycling of interfacial properties and charge-transfer kinetics of the Sn-C|NCAM full-cell, EIS analysis is performed in Fig. 4. The related Nyquist plots at the OCV and after 1, 8, and 10 galvanostatic cycles at the discharged state of the cell (voltage = 1 V) are collected in Fig. 4a. All the spectra reveal a low-frequency line typical of diffusion and middle-to-high-frequency semicircle(s) typical of interfacial processes. The low-frequency region, simulated by WQ_W elements, has been subtracted from the overall response to achieve the plots of Fig. 4b, with the aim of better evidencing the middle-to-high frequency features related to interfacial kinetics and to meet the boundary conditions ($\omega \rightarrow 0$) required for the subsequent calculation of DRT function with Tikhonov regularization [47–50]. Fig. 4a reveals two semicircles at middle-to-high frequencies, so that the overall Nyquist plots can be modeled to an equivalent circuit $R_{el}(R_1Q_1)(R_2Q_2)WQ_W$ in Boukamp's notation [47,48]. Although the individual anode and cathode contributions to the overall cell polarization cannot be properly discerned in the response of the full-cell in Figs. 4a,b, the two evidenced semicircles can be likely related with anode and cathode SEIs ($R_{SEI}Q_{SEI}$) at higher frequencies, and to charge-transfer processes ($R_{ct}Q_{dl}$) at lower frequencies, along with the electrolyte resistance (R_{el}) detected at the highest-frequency intercept with the real axis. The middle-to-high frequency dispersions in Fig. 4b have been fitted according to the equivalent circuit $R_{el}(R_{SEI}Q_{SEI})(R_{ct}Q_{dl})$, and the results displayed in Table 1 and Fig. 4c, which clearly show, after the cell formation cycle, a progressive increase of all resistances upon cycling. The increase of R_{el} value from the 1st to the 8th cycle indicates a progressive consumption of the electrolyte by side reactions, whose products can threaten the cell stability, thicken the interphases, and increase R_{SEI} and R_{ct}. At the 10th cycle, both R_{el} and R_{SEI} abruptly rise-up, thus indicating a worsening of the interfaces and, consequently, of the charge-transfer kinetics. Overall, from the 1st to the 10th cycle, R_{SEI} and R_{ct} respectively raised by 129 % and 210 %, further suggesting the need for a better selection of the cell setup to avoid its failure. It is worth noting that the decrease of R_{ct} during the first cycle is likely due to SEI partial dissolution, which is a known phenomenon in Na-ion cells [58]. Indeed, as the EIS measurements are performed at the discharged state of the full-cell (de-sodiated anode), some degree of SEI dissolution can occur in

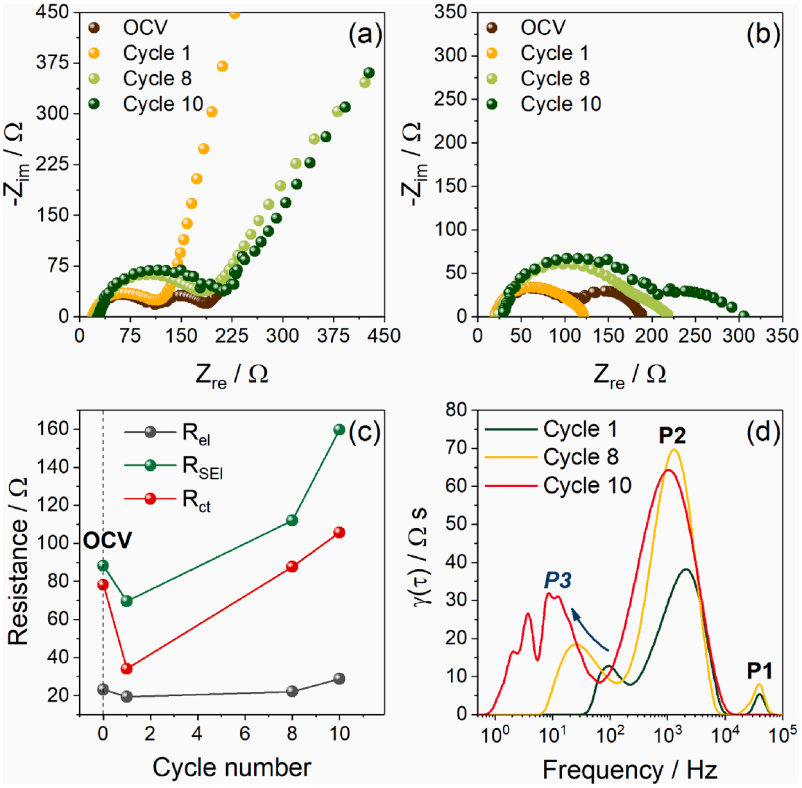

Fig. 4. EIS analysis of the Sn-C|NCAM three electrode full-cell. (a) Nyquist plots collected at the OCV of the cell and after 1, 8, and 10 galvanostatic cycles and (b) corresponding plots after subtraction of the diffusive contribute. (c) Trend of R_{el}, R_{SEI}, and R_{ct} as a function of the cycle number obtained from NLLS analysis of the impedance spectra. (d) DRT analyses in terms of γ-factor vs. frequency with associated peak indexing obtained from the Nyquist plot after 1, 8, and 10 galvanostatic cycles. EIS collected in the 500 kHz – 100 mHz frequency range with an alternate voltage signal of 30 mV. DRT calculations performed according to Tikhonov regularization with an optimal λ-value of 0.1 and assuming a Gaussian distribution. Room temperature (25 °C). See Materials and methods section for acronyms.

Table 1
NLLS analysis of the Nyquist plots reported in Fig. 4b recorded by performing EIS on Sn-C|NCAM full-cell using an additional Na electrode as reference, after subtraction of the diffusive contribution from Nyquist plot of Fig. 4a. Only fits with a χ^2 value of the order of 10^{-4} or lower were considered suitable [47,48]. See Materials and methods section for acronyms.

Cell condition	Equivalent circuit	R_{el} (Ω)	R_{SEI} (Ω)	R_{ct} (Ω)	χ^2
OCV	$R_{el}(R_{SEI}Q_{SEI})(R_{ct}Q_{dl})$	23.2 ± 0.3	88 ± 3	78 ± 2	4×10^{-4}
After 1 cycle	$R_{el}(R_{SEI}Q_{SEI})(R_{ct}Q_{dl})$	19.4 ± 0.1	70 ± 4	34 ± 4	4×10^{-5}
After 8 cycles	$R_{el}(R_{SEI}Q_{SEI})(R_{ct}Q_{dl})$	22.1 ± 0.2	112 ± 4	88 ± 5	9×10^{-5}
After 10 cycles	$R_{el}(R_{SEI}Q_{SEI})(R_{ct}Q_{dl})$	28.6 ± 0.4	160 ± 8	106 ± 15	6×10^{-4}

the initial cycling at the negative side, resulting in a decreased R_{SEI} (from 88 Ω to 70 Ω). Since the SEI can act as a barrier to overcome, its decreased thickness can improve charge transfer, thus limiting the R_{ct} at the anode side. After the initial cycles, the SEI consolidates and keeps increasing as above discussed, leading to electrolyte depletion and increasing R_{SEI} and R_{ct} [58]. The calculated DRT functions (Fig. 4d), with an optimized λ-value of 0.1 (see **Fig. S3** in Supporting Information), deconvolutes the different semicircles into peaks according to their relaxation frequencies [50]. Beside the minor peak labelled as *P*1 in the high-frequency region ($f > 10^4$ Hz) related with contribution from particle-particle and particle-current collector contact resistance, two main peaks can be clearly discerned at the 1st cycle: the peak labelled as *P*2 ($f \approx 10^3$ Hz) related with R_{SEI}, and the peak labelled as *P*3 ($f \approx 10^2$ Hz) related with R_{ct}. Both contributions increase progressively in intensity upon cycling, proportionally to the diameters of the associated semicircles, and *P*3 shifts to lower frequencies more markedly. For sake of clarity, the scattered Nyquist dispersion at the 10th cycle makes the gaussian distribution of *P*3 quite noisy; nevertheless, a clear shift from the previous cycles can be identified, thus suggesting worsening kinetics that progressively hinder the electrochemical processes. Although these results cannot fully discern the degradation mechanism in the cell, we may reasonably assume that parasitic reactions ascribed to the electrolyte can actually worsen the electrode/electrolyte interphases. Furthermore, the anode and cathode EIS contributions, separately collected using the additional Na-reference, are plotted in **Fig. S4** (Supporting Information). The results of the related fits by Equivalent Circuit method are summarized in **Tab. S1** and **Tab. S2** and are consistent with those obtained with the analysis of full-cell polarization.

To partially exclude the electrode structural deterioration or malfunctioning upon full-cell operation, we have collected in Fig. 5 SEM images of the pristine NCAM (panels **a, b**) and Sn-C (panels **e, f**), as well as those of NCAM (panels **c, d**) and Sn-C (panels **g, h**) taken from a cell cycled at 15 mA g_{cat}^{-1}. The NCAM before cycling shows a micrometric morphology (Fig. 5a) which reveals the submicron layers of the material when the magnification is increased (Fig. 5b) [10]. Furthermore, the cycled NCAM electrode evidences similar morphology at the lower magnification (Fig. 5c), however with a surface covered by electrolyte decomposition products forming the SEI, whilst the higher magnification image (Fig. 5d) still reveals the layers staking of the material which remains almost unaltered. On the other side, the pristine Sn-C shows the micrometric particles of the glassy carbon formed by resorcinol-formaldehyde annealing (Fig. 5e), and some nanometric Sn particles embedded in its surface at higher magnification (Fig. 5c) [45]. Despite the morphological similarity, the SEM of Sn-C after cycling highlights a rougher and more porous surface compared to the pristine state, with some bright spots typically triggered by a lower material conductivity (Fig. 5 g), and clear signs of side product precipitation in the SEI (Fig. 5h). These features well suggest the electrode structural stability and indicate once more the relevant presence of by-products likely precipitated at the electrode surface by electrolyte decomposition, further suggesting a better tuning of the electrolyte to improve the full-cell performance. This process appears more evident at the anode side rather than the cathode, as already indicated by the substantial increase of the interface resistance of Sn-C side of the full-cell (**Tab. S2**) compared to NCAM (**Tab. S1**), and confirmed by EIS analysis of the full-cell (see Fig. 4).

The preliminary results obtained for the Sn-C|NCAM full-cell clearly show the necessity of a dedicated experimental setup to stabilize the electrode/electrolyte mutual interactions. In this regard, a cathodic electrochemical stability window (C-ESW) of the electrolyte is assessed on a Na|SP-Cu cell and the results reported in **Fig. S5** (Supporting Information). The measurement reveals the occurrence of irreversible processes below 1.5 V vs. Na^+/Na ascribed to FEC reduction and SEI formation in the first cycle [58,59], as well as side voltammetry waves at about 0.9 V vs. Na^+/Na during the whole measurement, possibly due to electrolyte reduction. We may reasonably suppose that this undesired process is even more relevant at low current rates, such as those used in the full-cell in Fig. 3 [60]. These side reactions, already mentioned to justify the limited SEI stability revealed by EIS measurements in Fig. 4, are likely responsible for the low efficiency of the full-cell in Fig. 3. In order to check the individual behavior of NCAM and Sn-C, the electrodes are cycled in half sodium cells at the constant rates of 50 and 100 mA g^{-1}, respectively, as shown in **Fig. S6** (Supporting Information). The voltage profiles of the NCAM electrode evidence the Na-(de)intercalation in the layered structure, between 2.2 and 4.2 V (**Fig. S6a**), with an initial charge capacity of about 87 mAh g^{-1}, that is the 58 % of the one ascribed to the subsequent discharge (151 mAh g^{-1}). The difference between first charge and first discharge capacity is attributed to the Na-deficient character of the P3/P2-type layered oxide, which has the chemical formula $Na_{0.48}Al_{0.03}Co_{0.18}Ni_{0.18}Mn_{0.47}O_2$ [10]. The half-cell using NCAM reveals an efficiency exceeding 97 % after initial cycles, with a retention of about 64 % over 100 cycles (**Fig. S6b**). In contrast, the Sn-C anode activated for 2 h (**Fig. S6c**) exceeds the reduction degree expected by Fig. 1b, and reveals an almost fully-sodiated state of the electrode rather than a partially sodiated one. As mentioned in the experimental section, this outcome suggests that the activation actually depends on the material loading and the experimental setup, which require further tuning to allow the full control of the process. Furthermore, the voltage profiles show the typical sloping behavior and characteristic signatures ascribed with the Na-Sn alloying and Na insertion into the amorphous carbon, with a reversible capacity of about 80 mAh g^{-1} [17,30,31]. The corresponding cycling trend in **Fig. S6d** reveals a coulombic efficiency fluctuating between 96 % and 98 % after the first cycle, which leads to a capacity retention of about 73 % over 100 cycles. Considering the results of the half-cells, an optimization of the full-cell setup to increase the stability and the cycle life is carried out and the results are reported in Fig. 6. The figure shows the galvanostatic cycling of three different Sn-C|NCAM full-cells at a constant current increased up to 120 mA g^{-1} instead of 15 mA g_{cat}^{-1} (Fig. 3), and within various voltage setups adopted to limit the electrolyte decomposition and increase the cell efficiency and cycle life. Fig. 6a–c shows the voltage profiles of the cells cycled in the 1.5 – 4.5 V with an additional constant voltage step at 4.5 V until a current value of 12 mA g^{-1} is reached (CCCV mode), 1.0 – 4.1 V, and 1.0 – 4.0 V voltage ranges, respectively, while Fig. 6d depicts the cycling trends and coulombic efficiency of the three cells. It is worth noting that a 30 min activation rather than a longer step, such as that previously adopted for the preliminary full-cell, is carried out on the Sn-C anode due to the loading effect on the activation time already mentioned. The voltage profiles of the three cells reveal the combination of anode and cathode features, with the partial de-sodiation of Na-deficient NCAM and of the concomitant sodiation of Sn-C. The cell cycled up to 4.5 V (Fig. 6a) presents the higher maximum capacity of about 130 mAh g^{-1}, despite a low coulombic efficiency under 95 % in the initial cycles which decreases to 75 % after 100 cycles, leading to a rapid capacity fade to 20 mAh g^{-1} already after 50 cycles

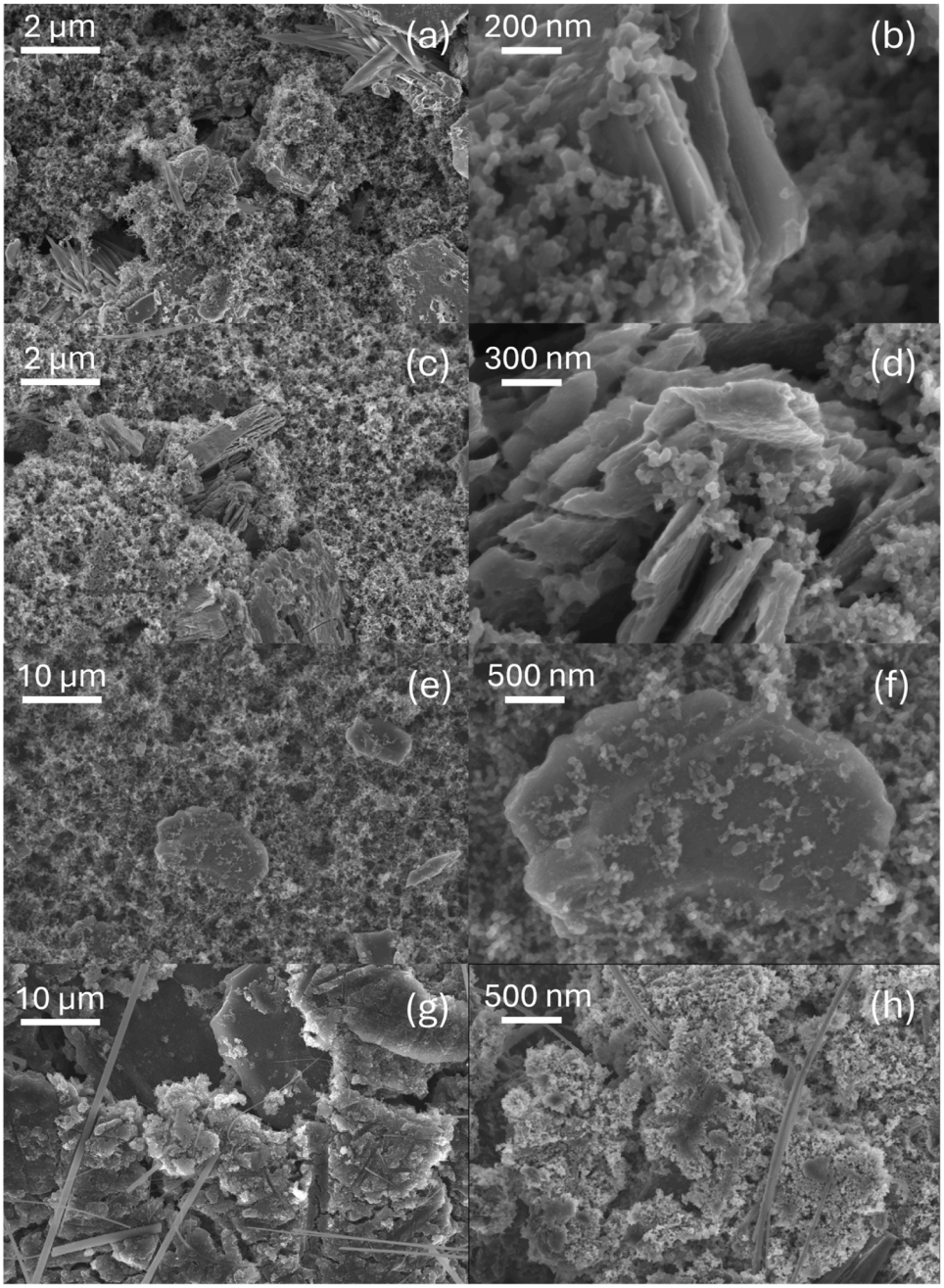

Fig. 5. SEM images of pristine (a, b) NCAM and (e, f) Sn-C electrodes and of (c, d) NCAM and (g, h) Sn-C electrodes recovered upon the cycling test at 15 mA g_{cat}^{-1} on a Sn-C|NCAM full-cell in the 1.0 – 4.5 V voltage range with an additional constant voltage step at 4.5 V (CCCV mode) until a final current of 3.75 mA g_{cat}^{-1} was reached. Room temperature (25 °C). See Materials and methods section for acronyms.

(green dots in Fig. 6d). This behavior may be ascribed to the above mentioned parasitic reactions of the electrolyte at low potential at the anode side, which can reach value approaching 0 V as triggered by the relatively high voltage of the full cell and the CCCV mode [53]. To limit this drawback, the CCCV mode is avoided and the upper voltage cut-off lowered to 4.1 V (Fig. 6b), and subsequently to 4.0 V (Fig. 6c). The corresponding cells reveal a lower maximum capacity of about 110 mAh g^{-1} and 101 mAh g^{-1}, respectively, compared to the one cycled at a higher cutoff, however with an increase of coulombic efficiency and stability. Indeed, both cells show a coulombic efficiency higher than 98 % for the whole test, with a capacity retention of 48 % for the cell up to 4.1 V (orange dots in Fig. 6d) and of 57 % for the cell up to 4.0 V (blue dots in Fig. 6d). Therefore, the obtained results suggest the narrowing of the voltage window and the use of high current rates as suitable setup to limit the parasitic reactions and increase the efficiency and stability of the resulting full-cell.

The galvanostatic performance of the optimized Sn-C|NCAM full-cell are reported in Fig. 7. Initially, the rate capability of the cell is evaluated in terms of voltage profiles (Fig. 7a) and the cycling trend (Fig. 7b) by increasing the current from 1 C to 5 C (1 $C = 50$ mA g^{-1}) in the 1.0 – 4.0 V voltage range, which is the one providing the best performance in Fig. 6. The cell reveals the expected shape of the voltage profiles influenced by the various C-rates, characterized by the combination of Sn-C and NCAM features, as already described (see discussion of Fig. 6). Furthermore, the profiles of Fig. 7a suggest an increase of the ohmic polarization by raising the current which leads to the decrease of capacity from 120 mAh g_{cat}^{-1} at 1 C to a still relevant value of 80 mAh g_{cat}^{-1} at 5 C. On the other hand, the cycling trend of Fig. 7b depicts that the initial capacity is

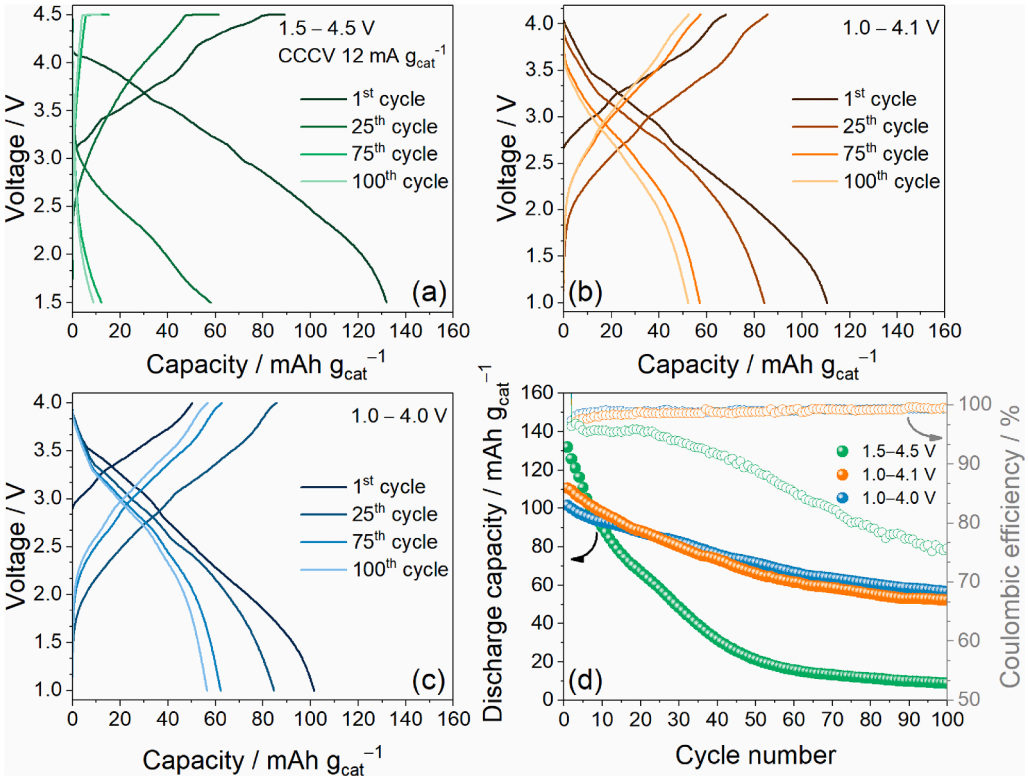

Fig. 6. Galvanostatic cycling tests of Sn-C|NCAM full-cells adopting different voltage ranges at the constant current rate of 120 mA g_{cat}^{-1}. In detail: (a-c) selected voltage profiles, and (d) discharge capacity trends reporting coulombic efficiencies on right-hand side *y*-axis. Voltage ranges: 1.5 – 4.5 V with an additional constant voltage step at 4.5 V (CCCV mode) until a final current of 12 mA g_{cat}^{-1} (green); 1.0 – 4.1 V (orange); 1.0 – 4.0 V (blue). Electrodes loading (NCAM and Sn-C, respectively): 3.73 mg cm^{-2} and 5.53 mg cm^{-2} (green), 2.0 mg cm^{-2} and 4.0 mg cm^{-2} (orange), 2.1 mg cm^{-2} and 3.4 mg cm^{-2} (blue). Sn-C activated for 30 min timeframe. Room temperature (25 °C). See Materials and methods section for acronyms.

almost completely recovered by decreasing the current back to 1 C (~ 108 mAh g_{cat}^{-1}) after the whole test, and that the increase of the current raises the coulombic efficiency over 98 % since the parasitic reactions are mitigated as mentioned above [58]. This aspect suggests again the use of high current instead of the low one to trigger the capacity retention of the full-cell [61]. Nevertheless, the trend of Fig. 7b suggests a good rate capability and stability of the optimized cell configuration upon the stress caused by raising the currents. To further investigate the interfacial stability of the optimized —Sn-C|NCAM full-cell, EIS measurements are performed before and after the rate capability test, and the results reported in **Fig. S7** (Supporting Information). The Nyquist plots are modeled to an equivalent circuit $R_{el}(R_{SEI}Q_{SEI})(R_{ct}Q_{dl})WQ_W$ in Boukamp's notation [47,48], and the fitting results displayed in **Tab. S3**.

The results reveal the stabilization of the electrode/electrolyte interphase in the optimized cell, however with a slightly higher increase of the R_{ct} compared to the cell of Fig. 4 (i.e., 280 % rather than 210 %), which is possibly due to the increased materials stress driven by the rate capability test. Nevertheless, the obtained stability of the electrolyte and the SEI is ascribed to the optimized full-cell setup and testing conditions when compared to the trends observed in Fig. 4. Gravimetric energy density and power density (Fig. 7c) are calculated from the rate capability test integrating the capacity or the current as a function of the cell voltage, respectively, and normalizing by the mass of the cathode active material (the average discharge voltage was employed for the power density). The cell reveals an initial energy density at 1 C of about 300 Wh kg_{cat}^{-1}, which decreases as the current increases, whilst the power density raises concomitantly to reach a maximum value of about 650 W kg_{cat}^{-1} at 5C. These high values can actually reflect lower, but still relevant, gravimetric energy and power densities of the entire Na-ion battery, as normalized to the whole mass including anode, electrolyte, and other inactive components (e.g. current collectors, separator, cell casing). Nevertheless, the results of the optimized full-cell, especially in terms of energy density, are promising if compared to other cells employing hard carbon as anode material combined with layered oxide cathodes (see **Table S4** in Supporting Information). Hence, the Sn-C|NCAM full-cell reaches energy density of 300 Wh kg_{cat}^{-1} at a current of 50 mA g^{-1}, which is higher than that achieved by some literature examples such as the HC|$Na[Li_{0.05}Mn_{0.5}Ni_{0.3}Cu_{0.1}Mg_{0.05}]O_2$ cell (i.e., 215 Wh kg^{-1} at 20 mA g^{-1}) [62], the HC|O3-$Na_{0.9}[Cu_{0.22}Fe_{0.30}Mn_{0.48}]O_2$ cell (i.e., 210 Wh kg^{-1} at 10 mA g^{-1}) [63], and the C|$NaFe_{0.5}Mn_{0.5}O_2$+10 %wtNa_3P cell (i.e., 210 Wh kg^{-1} at 20 mA g^{-1}) [64]. Furthermore, the obtained values are well competing if compared with full-cells employing different cathodes requiring pre-sodiation, such as the polyanionic one in the NPUCS|NVPF cell (136 Wh kg^{-1} at 100 mA g^{-1}) [65], and the Prussian blue in the PAQS|Na1.78MnFe$(CN)_6$ × 2·$3H_2O$ cell (100 Wh kg^{-1} at 34 mA g^{-1}) [66]. Relevantly, our full-cell holds the promising energy density of 205 Wh Kg_{cat}^{-1} even at a current as high as 250 mA g^{-1}. These outcomes suggest the use of the chemically sodiated alloying Sn-C anode to improve the energy density of the Na-ion full-cell. With the aim of further studying the lifespan, a long term cycling test of the Sn-C|NCAM full-cell is carried out at the constant current rate of 200 mA g_{cat}^{-1} in the 1.0 – 4.0 V voltage range, with an additional constant voltage step at 4.0 V until a final current of 50 mA g_{cat}^{-1}. The voltage profiles (Fig. 7d) show the well-defined combination of anode and cathode features, and a maximum capacity of 85 mAh g_{cat}^{-1}, in agreement with the rate capability test. The cell also depicts a coulombic efficiency approaching 100 % after initial cycles, and a capacity retention of 55 % after 250 charge/-discharge runs (Fig. 7e), thus confirming the key role of the electrolyte stability and the anode chemical activation to get a relevant performance of the Na-ion full-cell.

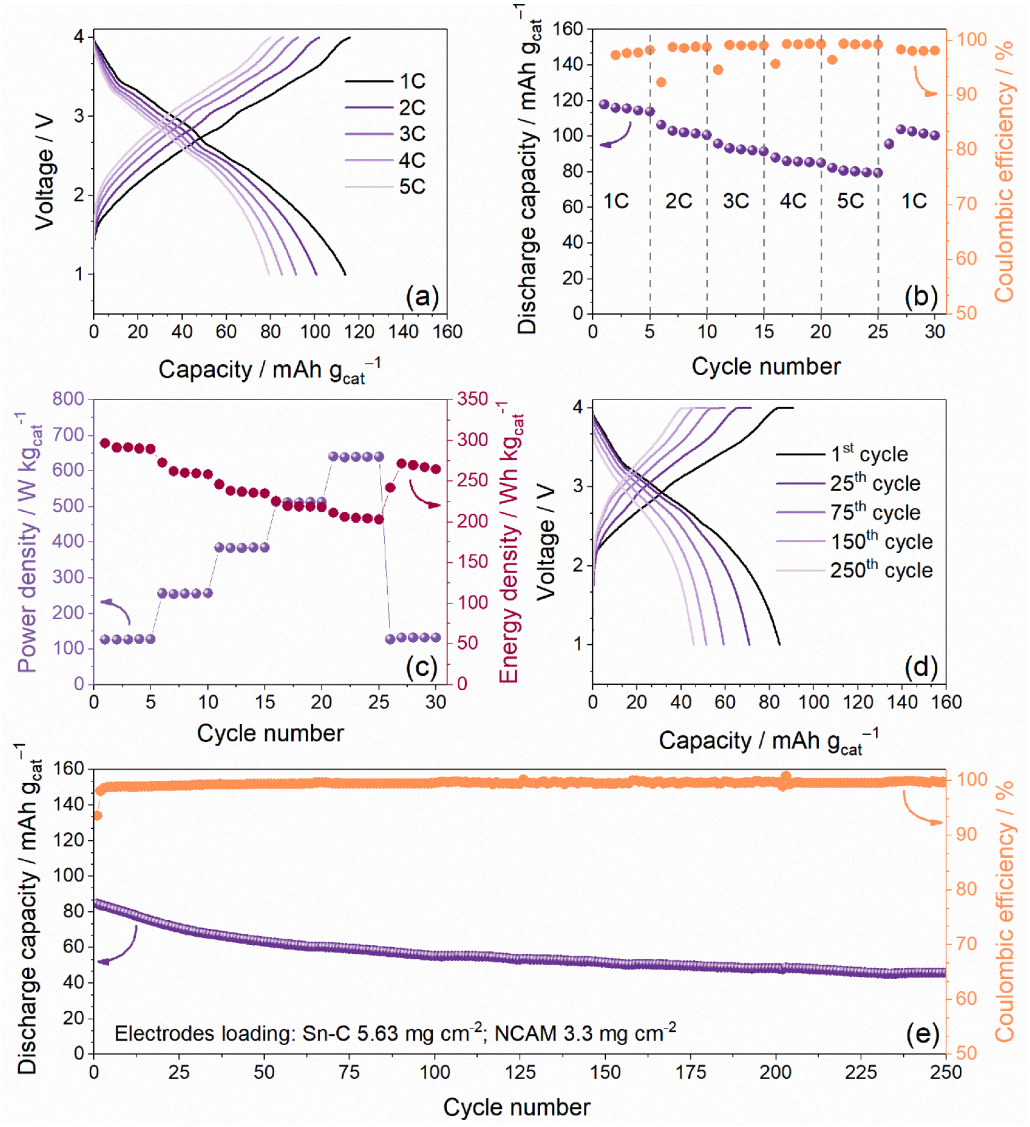

Fig. 7. Electrochemical performance of optimized Sn-C|NCAM full-cell. Rate capability test in terms of (a) selected voltage profiles (5th for each current rate) and (b) discharge capacity trend reporting coulombic efficiencies on right-hand side *y*-axis. Test performed at 1 C, 2 C, 3 C, 4 C, and 5 C currents (1C = 50 mA g_{cat}^{-1}). Voltage range 1.0 – 4.0 V. (c) Trend of calculated power density and energy density obtained from the rate capability test results. Long-term cycling test at the constant current of 200 mA g_{cat}^{-1} in terms of (d) selected voltage profiles and (e) discharge capacity trend reporting coulombic efficiencies on right-hand side *y*-axis started after the rate capability test. Voltage range 1.0 – 4.0 V with an additional constant voltage step at 4.0 V (CCCV mode) until a final current of 50 mA g_{cat}^{-1}. Sn-C activated for 30 min timeframe. Room temperature (25 °C). See Materials and methods section for acronyms.

4. Conclusions

In this work we exploited the pre-treatment process of a Sn-C anode for achieving its efficient operation as the alloying electrode in Na-ion battery in combination with a NCAM layered cathode. The treatment consisted of direct Sn-C chemical sodiation by capillary contact of the electrode with Na metal, controlling time and pressure, especially considering active material loading, to properly tune the alkali metal content in the electrode. XRD, Raman spectroscopy, SEM/EDS analysis, and electrochemical tests have shown the achievement of different sodiation degrees in the anode by changing the activation time, which can allow its combination with various Na-deficent cathodes, such as the layered oxides, in full-cell configuration. Hence, a Sn-C|NCAM cell was initially tested with N/P ratio of 1.1 and subjected to charge/discharge tests at 15 mA g_{cat}^{-1} showing reversible voltage profiles for only 10 cycles. The cell revealed an initial capacity as high as 150 mAh g_{cat}^{-1} and a final one of about 110 mAh g^{-1}, with a coulombic efficiency fluctuating from 51 to 85 %. The relatively low efficiency leading to the above short cycling has been ascribed to side reactions of the electrodes with the electrolyte, in particular at the anode side, confirmed by the C-ESW of the electrolyte, by the EIS measurements and DRT calculation performed on the full-cell. The above tests indicated an increase of about 129 % of the SEI resistance, and of 210 % of the charge-transfer one, as confirmed by the increase in intensity and concomitant shift to lower frequencies of the DRT peaks. This behavior suggested worsening of the reaction kinetics by cycling, and the need for better tuning of the cell and the galvanostatic cycling conditions to achieve higher efficiency and stability. On the other hand, ex-situ SEM analysis of Sn-C and NCAM have shown the structural integrity of the electrodes upon cycling, which has instead promoted the electrolyte decomposition and precipitation of side product at the surface, principally at the anode one. These preliminary outcomes allowed the optimization of the Sn-C|NCAM full-cell setup to avoid the side reactions by better tuning its balance, increasing the current rate, and narrowing the voltage window. Indeed, the optimized full-cell revealed a rate capability extended up to 5 C (1 C = 50 mAh g_{cat}^{-1}), with improved electrode/electrolyte interphase stability and

promising maximum energy and power densities of 300 Wh kg_{cat}^{-1} and 650 W kg_{cat}^{-1}, respectively. Furthermore, the cell revealed a stability increased to 250 charge/discharged cycles at 200 mA g_{cat}^{-1} with a maximum capacity of 85 mAh g_{cat}^{-1} and good retention. The obtained results suggested the direct chemical anode sodiation adopted in this work as suitable approach to achieve full Na-ion battery with promising performances in terms of efficiency and stability, which is proposed for a sustainable energy storage.

CRediT authorship contribution statement

Luca Minnetti: Conceptualization, Data curation, Formal analysis, Investigation, Methodology, Writing – original draft. **Edoardo Barcaro:** Conceptualization, Formal analysis, Investigation, Visualization, Writing – original draft, Data curation. **Leonardo Sbrascini:** Investigation, Methodology, Writing – original draft. **Francesco Nobili:** Software, Supervision, Visualization, Writing – review & editing. **Jusef Hassoun:** Conceptualization, Data curation, Formal analysis, Funding acquisition, Investigation, Methodology, Project administration, Supervision, Writing – original draft, Writing – review & editing.

Declaration of competing interest

The authors declare that they have no known competing financial interests or personal relationships that could have appeared to influence the work reported in this paper.

Acknowledgments

The work was performed within the grant “Fondo di Ateneoper la Ricerca Locale (FAR) 2024″, University of Ferrara, and the collaboration project “Accordo di Collaborazione Quadro 2015” between University of Ferrara (Department of Chemical and Pharmaceutical Sciences) and Sapienza University of Rome (Department of Chemistry). Project funded under the National Recovery and Resilience Plan (NRRP), Mission 04 Component 2 Investment 1.5 – NextGenerationEU, Call for tender n. 3277 dated 30/12/2021, Award Number: 0001052 dated 23/06/2022.

Supplementary materials

Supplementary material associated with this article can be found, in the online version, at doi:10.1016/j.materresbull.2025.113546.

Data availability

Data will be made available on request.

References

[1] B. Scrosati, J. Garche, Lithium batteries: status, prospects and future, J. Power Sources 195 (2010) 2419–2430.
[2] D. Di Lecce, R. Verrelli, J. Hassoun, Lithium-ion batteries for sustainable energy storage: recent advances towards new cell configurations, Green Chem. 19 (2017) 3442–3467.
[3] N. Yabuuchi, K. Kubota, M. Dahbi, S. Komaba, Research development on sodium-ion batteries, Chem. Rev. 114 (2014) 11636–11682.
[4] I. Hasa, J. Hassoun, S. Passerini, Nanostructured Na-ion and Li-ion anodes for battery application: a comparative overview, Nano Res. 10 (2017) 3942–3969.
[5] K. Kubota, N. Yabuuchi, H. Yoshida, M. Dahbi, S. Komaba, Layered oxides as positive electrode materials for Na-ion batteries, MRS Bull. 39 (2014) 416–422.
[6] S. Komaba, N. Yabuuchi, T. Nakayama, A. Ogata, T. Ishikawa, I. Nakai, Study on the reversible electrode reaction of $Na_{1-x}Ni_{0.5}Mn_{0.5}O_2$ for a rechargeable sodium-ion battery, Inorg. Chem. 51 (2012) 6211–6220.
[7] N. Yabuuchi, R. Hara, M. Kajiyama, K. Kubota, T. Ishigaki, A. Hoshikawa, S. Komaba, New O2/P2-type Li-excess layered manganese oxides as promising multi-functional electrode materials for rechargeable Li/Na batteries, Adv. Energy Mater. 4 (2014) 1301453.
[8] H. Yoshida, N. Yabuuchi, K. Kubota, I. Ikeuchi, A. Garsuch, M. Schulz-Dobrick, S. Komaba, P2-type $Na_{(2/3)}Ni_{(1/3)}Mn_{(2/3-x)}Ti_{(x)}O_2$ as a new positive electrode for higher energy Na-ion batteries, Chem. Comm. 50 (2014) 3677–3680.
[9] M.H. Han, E. Gonzalo, G. Singh, T. Rojo, A comprehensive review of sodium layered oxides: powerful cathodes for Na-ion batteries, Energy Environ. Sci. 8 (2015) 81–102.
[10] D. Di Lecce, D. Campanella, J. Hassoun, Insight on the enhanced reversibility of a multimetal layered oxide for sodium-ion battery, J. Phys. Chem. C 122 (2018) 23925–23933.
[11] D. Di Lecce, S. Levchenko, F. Iacoviello, D.J.L. Brett, P.R. Shearing, J. Hassoun, X-ray nano-computed tomography of electrochemical conversion in lithium-ion battery, ChemSusChem. 12 (2019) 3550–3561.
[12] Y.M. Xin, A review on application of $LiFePO_4$ based composites as electrode materials for Lithium Ion batteries, Int. J. Electrochem. Sci. 16 (6) (2021) 210655.
[13] V. Marangon, L. Minnetti, E. Barcaro, J. Hassoun, Room-temperature solid-State polymer electrolyte in Li-$LiFePO_4$, Li-S and Li-O_2 batteries, Chem. Eur. J. 29 (2023) e202301345.
[14] C. Tealdi, J. Heath, M.S. Islam, Feeling the strain: enhancing ionic transport in olivine phosphate cathodes for Li- and Na-ion batteries through strain effects, J. Mater. Chem. A Mater. 4 (2016) 6998–7004.
[15] S. Qiao, Synthesis and electrochemical properties of Na and Mg co- doped $LiFe_{0.65}Mn_{0.35}PO_4$/C cathode materials for lithium-ion batteries, Int. J. Electrochem. Sci. 14 (2019) 11616–11629.
[16] L. Minnetti, L. Sbrascini, A. Staffolani, V. Marangon, F. Nobili, J. Hassoun, Unravelling the ion transport and the interphase properties of a mixed olivine cathode for Na-ion battery, J. Energy Chem. 96 (2024) 300–317.
[17] I. Hasa, J. Hassoun, Y.K. Sun, B. Scrosati, Sodium-ion battery based on an electrochemically converted $NaFePO_4$ cathode and nanostructured tin-carbon anode, Chemphyschem. 15 (2014) 2152–2155.
[18] M. Marinaro, M. Weinberger, M. Wohlfahrt-Mehrens, Toward pre-lithiatied high areal capacity silicon anodes for Lithium-ion batteries, Electrochim. Acta 206 (2016) 99–107.
[19] E. Barcaro, V. Marangon, M. Mutarelli, J. Hassoun, A lithium-ion battery with cycling stability promoted by the progressive activation of a silicon oxide anode in graphene-amorphous carbon matrix, J. Power Sources 595 (2024) 234059.
[20] M. Haruta, T. Moriyasu, A. Tomita, T. Takenaka, T. Doi, M. Inaba, Pre-film formation and cycle performance of silicon-flake-powder negative electrode in a solvate ionic liquid for silicon-sulfur rechargeable batteries, J. Electrochem. Soc. 165 (2018) A1874–A1879.
[21] L. Minnetti, V. Marangon, P. Andreotti, A. Staffolani, F. Nobili, J. Hassoun, Reciprocal irreversibility compensation of $LiNi_{0.2}Co_{0.2}Al_{0.1}Mn_{0.45}O_2$ cathode and silicon oxide anode in new Li-ion battery, Electrochim. Acta 452 (2023) 142263.
[22] A.R. Kamali, D.J. Fray, Tin-based materials as advanced anode materials for lithium ion batteries: a review, Rev. Adv. Mater. Sci. 27 (2011) 14–24.
[23] S.M. Oh, S.T. Myung, M.W. Jang, B. Scrosati, J. Hassoun, Y.K. Sun, An advanced sodium-ion rechargeable battery based on a tin–carbon anode and a layered oxide framework cathode, Phys. Chem. Chem. Phys. 15 (2013) 3827.
[24] C.M. Park, S. Yoon, S.I. Lee, J.H. Kim, J.H. Jung, H.J. Sohn, High-rate capability and enhanced cyclability of antimony-based composites for lithium rechargeable batteries, J. Electrochem. Soc. 154 (2007) A917–A920.
[25] M. He, K. Kravchyk, M. Walter, M.V. Kovalenko, Monodisperse antimony nanocrystals for high-rate Li-ion and Na-ion battery anodes: nano versus bulk, Nano Lett. 14 (2014) 1255–1262.
[26] J. Hassoun, G. Derrien, S. Panero, B. Scrosati, A SnSb–C nanocomposite as high performance electrode for lithium ion batteries, Electrochim. Acta 54 (2009) 4441–4444.
[27] I. Hasa, S. Passerini, J. Hassoun, A rechargeable sodium-ion battery using a nanostructured Sb-C anode and P2-type layered $Na_{0.6}Ni_{0.22}Fe_{0.11}Mn_{0.66}O_2$ cathode, RSC Adv. 5 (2015) 48928.
[28] L. Sbrascini, A. Staffolani, L. Bottoni, H. Darjazi, L. Minnetti, M. Minicucci, F. Nobili, Structural and interfacial characterization of a sustainable Si/hard carbon composite anode for lithium-ion batteries, ACS Appl. Mater. Interfaces 14 (2022) 33257–33273.
[29] D.Y.W. Yu, P.V. Prikhodchenko, C.W. Mason, S.K. Batabyal, J. Gun, S. Sladkevich, A.G. Medvedev, O. Lev, High-capacity antimony sulphide nanoparticle-decorated graphene composite as anode for sodium-ion batteries, Nat. Commun. 4 (2013) 2922.
[30] S. Komaba, Y. Matsuura, T. Ishikawa, N. Yabuuchi, W. Murata, S. Kuze, Redox reaction of Sn-polyacrylate electrodes in aprotic Na cell, Electrochem. commun. 21 (2012) 65–68.
[31] B. Zhang, G. Rousse, D. Foix, R. Dugas, D.A.D. Corte, J.M. Tarascon, Microsized Sn as advanced anodes in glyme-based electrolyte for Na-ion batteries, Adv. Mater. 28 (2016) 9824–9830.
[32] Y.C. Lu, C. Ma, J. Alvarado, T. Kidera, N. Dimov, Y.S. Meng, S. Okada, Electrochemical properties of tin oxide anodes for sodium-ion batteries, J. Power Sources 284 (2015) 287–295.
[33] H. Zhu, Z. Jia, Y. Chen, N. Weadock, J. Wan, O. Vaaland, X. Han, T. Li, L. Hu, Tin anode for sodium-ion batteries using natural wood fiber as a mechanical buffer and electrolyte reservoir, Nano Lett. 13 (2013) 3093–3100.
[34] L.D. Ellis, T.D. Hatchard, M.N. Obrovac, Reversible insertion of sodium in tin, J. Electrochem. Soc. 159 (2012). A1801–A1805.
[35] G. Liu, Z. Sun, X. Shi, X. Wang, L. Shao, Y. Liang, X. Lu, J. Liu, Z. Guo, 2D-Layer-structure Bi to quasi-1D-structure $NiBi_3$: structural dimensionality reduction to superior sodium and potassium ion storage, Adv. Mater. 35 (2023) 2305551.
[36] S. Lin, H. Zhang, C. Shu, W. Hua, X. Wang, Y. Zhao, J. Luo, Z. Tang, Y. Wu, W. Tang, Research progress and perspectives on pre-sodiation strategies for sodium-ion batteries, Adv. Funct. Mater. 34 (2024) 2409628.

[37] P. Kulkarni, H. Jung, D. Ghosh, M. Jalalah, M. Alsaiari, F.A. Harraz, R. G. Balakrishna, A comprehensive review of pre-lithiation/sodiation additives for Li-ion and Na-ion batteries, J. Energy Chem. 76 (2023) 479–494.
[38] W. Liu, X. Chen, C. Zhang, H. Xu, X. Sun, Y. Zheng, Y. Yu, S. Li, Y. Huang, J. Li, Gassing in Sn-anode sodium-ion batteries and its remedy by metallurgically prealloying Na, ACS. Appl. Mater. Interfaces. 11 (2019) 23207–23212.
[39] L. Hou, T. Liu, H. Wang, M. Bai, X. Tang, Z. Wang, M. Zhang, S. Li, T. Wang, K. Zhou, Y. Ma, Boosting the reversible, high-rate Na^+ storage capability of the hard carbon anode via the synergistic structural tailoring and controlled presodiation, Small. 19 (2023) 2207638.
[40] N. Qin, Y. Sun, C. Hu, S. Liu, Z. Luo, X. Cao, S. Liang, G. Fang, Boosting high initial coulombic efficiency of hard carbon by in-situ electrochemical presodiation, J. Energy Chem. 77 (2023) 310–316.
[41] Y. Niu, Y. Guo, Y. Yin, S. Zhang, T. Wang, P. Wang, S. Xin, Y. Guo, High-efficiency cathode sodium compensation for sodium-ion batteries, Adv. Mater. 32 (2020) 2001419.
[42] J.H. Jo, J.U. Choi, Y.J. Park, J.K. Ko, H. Yashiro, S.T. Myung, A new pre-sodiation additive for sodium-ion batteries, Energy Storage Mater. 32 (2020) 281–289.
[43] L. Sbrascini, A. Sarapulova, C. Gauckler, L. Gehrlein, F. Jeschull, T. Akçay, R. Mönig, M. Marinaro, F. Nobili, S. Dsoke, Effect of presodiation additive on structural and interfacial stability of hard carbon|P2-$Na_{0.66}Mn_{0.75}Ni_{0.2}Mg_{0.05}O_2$ full cell, Batter. Supercaps. 7 (2024) e202400207.
[44] J. Hassoun, P. Ochal, S. Panero, G. Mulas, C. Bonatto Minella, B. Scrosati, The effect of CoSn/$CoSn_2$ phase ratio on the electrochemical behaviour of $Sn_{40}Co_{40}C_{20}$ ternary alloy electrodes in lithium cells, J. Power Sources 180 (2008) 568–575.
[45] J. Hassoun, G. Derrien, S. Panero, B. Scrosati, A nanostructured Sn-C composite lithium battery electrode with unique stability and high electrochemical performance, Adv. Mater. 20 (2008) 3169–3175.
[46] D. DiLecce, V. Marangon, M. Isaacs, R. Palgrave, P.R. Shearing, J. Hassoun, Degradation of layered oxide cathode in a sodium battery: a detailed investigation by X-ray tomography at the nanoscale, Small Methods 5 (2021) 2100596.
[47] B. Boukamp, A nonlinear Least squares fit procedure for analysis of immittance data of electrochemical systems, Solid. State Ion 20 (1986) 31–44.
[48] B. Boukamp, A package for impedance/admittance data analysis, Solid. State Ion 18–19 (1986) 136–140.
[49] F. Ciucci, C. Chen, Analysis of electrochemical impedance spectroscopy data using the distribution of relaxation times: a bayesian and hierarchical bayesian approach, Electrochim. Acta 167 (2015) 439–454.
[50] A.L. Gavrilyuk, D.A. Osinkin, D.I. Bronin, The use of Tikhonov regularization method for calculating the distribution function of relaxation times in impedance spectroscopy, Russ. J. Electrochem. 53 (2017) 575–588.
[51] D.J. Lee, J.W. Park, I. Hasa, Y.K. Sun, B. Scrosati, J. Hassoun, Alternative materials for sodium ion–sulphur batteries, J. Mater. Chem. A Mater. 1 (2013) 5256.
[52] V. Marangon, E. Barcaro, F. De Boni, M. Prato, D. Bresser, J. Hassoun, Effective liquid electrolytes for enabling room-temperature sodium–Sulfur batteries, Adv. Sustain. Syst. 8 (2024) 2400268.
[53] L.Y. Kuo, A. Moradabadi, H.F. Huang, B.J. Hwang, P. Kaghazchi, Structure and ionic conductivity of the solid electrolyte interphase layer on tin anodes in Na-ion batteries, J. Power Sources 341 (2017) 107–113.
[54] J.S. Weaving, A. Lim, J. Millichamp, T.P. Neville, D. Ledwoch, E. Kendrick, P. F. McMillan, P.R. Shearing, C.A. Howard, D.J.L. Brett, Elucidating the sodiation mechanism in hard carbon by operando Raman spectroscopy, ACS Appl. Energy Mater. 3 (2020) 7474–7484.
[55] N. Phattharasupakun, P. Bunyanidhi, P. Chiochan, N. Chanlek, M. Sawangphruk, Effect of charging protocols on electrochemical performance and failure mechanism of commercial level Ni-rich NMC811 thick electrode, Electrochem. Commun. 139 (2022) 107309.
[56] S. Komaba, T. Ishikawa, N. Yabuuchi, W. Murata, A. Ito, Y. Ohsawa, Fluorinated ethylene carbonate as electrolyte additive for rechargeable Na batteries, ACS Appl. Mater. Interfaces. 3 (2011) 4165–4168.
[57] S. Komaba, W. Murata, T. Ishikawa, N. Yabuuchi, T. Ozeki, T. Nakayama, A. Ogata, K. Gotoh, K. Fujiwara, Electrochemical Na insertion and solid electrolyte interphase for hard-carbon electrodes and application to Na-ion batteries, Adv. Funct. Mater. 21 (2011) 3859–3867.
[58] M.Á. Muñoz-Márquez, D. Saurel, J.L. Gómez-Cámer, M. Casas-Cabanas, E. Castillo-Martínez, T. Rojo, Na-ion batteries for large scale applications: a review on anode materials and solid electrolyte interphase formation, Adv. Energy Mater. 7 (2017) 1700463.
[59] U. Purushotham, N. Takenaka, M. Nagaoka, Additive effect of fluoroethylene and difluoroethylene carbonates for the solid electrolyte interphase film formation in sodium-ion batteries: a quantum chemical study, RSC Adv. 6 (2016) 65232–65242.
[60] S. Alvin, H.S. Cahyadi, J. Hwang, W. Chang, S.K. Kwak, J. Kim, Revealing the intercalation mechanisms of lithium, sodium, and potassium in hard carbon, Adv. Energy Mater. 10 (2020) 2000283.
[61] M.J. Lain, J. Brandon, E. Kendrick, Design strategies for high power vs. high energy lithium ion cells, Batteries 5 (2019) 64.
[62] J. Deng, W. Bin Luo, X. Lu, Q. Yao, Z. Wang, H.K. Liu, H. Zhou, S.X. Dou, High energy density sodium-ion battery with industrially feasible and air-stable O3-type layered oxide cathode, Adv. Energy Mater. 8 (2018) 1701610.
[63] L. Mu, S. Xu, Y. Li, Y. Hu, H. Li, L. Chen, X. Huang, Prototype sodium-ion batteries using an air-stable and Co/Ni-free O3-layered metal oxide cathode, Adv. Mater. 27 (2015) 6928–6933.
[64] B. Zhang, R. Dugas, G. Rousse, P. Rozier, A.M. Abakumov, J.M. Tarascon, Insertion compounds and composites made by ball milling for advanced sodium-ion batteries, Nat. Commun. 7 (2016) 10308.
[65] S. Wu, H. Peng, J. Xu, L. Huang, Y. Liu, X. Xu, Y. Wu, Z. Sun, Nitrogen/phosphorus co-doped ultramicropores hard carbon spheres for rapid sodium storage, Carbon 218 (2024) 118756.
[66] X. Zhang, Y. Hong, T. Zhang, X. Ma, Y. Wei, Z. Zi, Z. Hou, Toward high-energy and long-cycle-life prussian blue-based aqueous sodium-ion batteries, ACS. Appl. Nano Mater. 8 (2025) 733–740.